HHS Public Access

Author manuscript

Nat Biomed Eng. Author manuscript; available in PMC 2023 May 01.

Published in final edited form as:

Nat Biomed Eng. 2022 May ; 6(5): 584–592. doi:10.1038/s41551-021-00735-8.

Massively parallel photoacoustic computed tomography of human brain function

Shuai Na[1,&], **Jonathan J. Russin**[2,3,4,&], **Li Lin**[1,&], **Xiaoyun Yuan**[1,5,&], **Peng Hu**[1], **Kay B. Jann**[6], **Lirong Yan**[6], **Konstantin Maslov**[1], **Junhui Shi**[1,7], **Danny J. Wang**[6], **Charles Y. Liu**[2,3,4,*], **Lihong V. Wang**[1,8,*]

[1]Caltech Optical Imaging Laboratory, Andrew and Peggy Cherng Department of Medical Engineering, California Institute of Technology, Pasadena, CA 91125, USA

[2]Department of Neurological Surgery, Keck School of Medicine, University of Southern California, Los Angeles, CA 90033, USA

[3]Neurorestoration Center, Keck School of Medicine, University of Southern California, Los Angeles, CA 90033, USA

[4]Rancho Los Amigos National Rehabilitation Center, Downey, CA 90242, USA

[5]Present address: Department of Electronic Engineering, Tsinghua University, Beijing 100084, China

[6]Laboratory of Functional MRI Technology, Stevens Neuroimaging and Informatics Institute, Keck School of Medicine, University of Southern California, Los Angeles, CA 90033, USA

[7]Present address: Zhejiang Lab, Hangzhou, China

[8]Caltech Optical Imaging Laboratory, Department of Electrical Engineering, California Institute of Technology, Pasadena, CA 91125, USA

[*]Corresponding authors, LVW@caltech.edu (L.V.W.); cliu@usc.edu (C.Y.L.), **Correspondence and requests for materials** should be addressed to L.V.W.

[&]These authors contributed equally

Author contributions

L.V.W., C.Y.L., and S.N. conceived the project. S.N., J.J.R., C.Y.L., and L.V.W. designed the study. L.L., S.N., K.M., and J.S. built the system hardware. S.N. developed the system software. S.N., X.Y., and J.J.R. performed the PACT experiments. K.B.J. and L.Y. performed the MRI experiments. P.H., X.Y., and S.N. developed the reconstruction algorithms. X.Y., S.N., K.B.J., J.J.R., C.Y.L., D.J.W., and L.V.W. analyzed and interpreted the data. J.J.R. and C.Y.L. recruited the subjects. S.N., J.J.R., and X.Y. wrote the manuscript with input from all authors. L.V.W., C.Y.L., and D.J.W. supervised the study.

Reporting summary.

Further information on research design is available in the Nature Research Reporting Summary linked to this article.

Code availability

The fMRI data were processed with freely available software package SPM12. The codes used to extract the fPACT function are available at https://doi.org/10.5281/zenodo.4615721. The reconstruction codes based on the universal backprojection algorithm, the system control software, and the data collection software are proprietary and used in licensed technologies, yet they are available from the corresponding authors on reasonable request.

Competing interests

L.V.W. has a financial interest in Microphotoacoustics, Inc., CalPACT, LLC, and Union Photoacoustic Technologies, Ltd., which, however, did not support this work. K.M. has a financial interest in Microphotoacoustics, Inc. The other authors declare no competing interests.

Peer review information *Nature Biomedical Engineering* thanks Reviewer and the other, anonymous, reviewer(s) for their contribution to the peer review of this work.

Abstract

Functional human brain imaging is mainly based on blood-oxygen-level-dependent (BOLD) functional magnetic resonance imaging (fMRI), which is a mature technology with recognized constraints in certain clinical and research applications. Photoacoustic computed tomography (PACT) is a promising complementary modality to fMRI as it does not involve magnetic fields and allows quantification of deoxyhemoglobin and oxyhemoglobin concentrations, convertible to oxygen saturation and blood volume. PACT has been explored in animal models but not in the human brain due to the limited field of view (FOV), imaging speed, sensitivity, and penetration depth. Here, we demonstrate PACT of the human brain using a massively parallel three-dimensional system with a 10-cm–diameter FOV and spatiotemporal resolution of 350 μm and 2 s. Functional PACT imaging was performed in post-hemicraniectomy patients and validated against 7 Tesla BOLD fMRI. Achieved functional results exhibit strong spatial correspondence in the same FOV and a high temporal correlation between hemoglobin and BOLD functional signals, however, with earlier detection of signal changes. Our findings demonstrate the potential of PACT for broader-scope human brain imaging.

Since its inception in 1990, blood-oxygen-level-dependent (BOLD) imaging, the primary form of functional magnetic resonance imaging (fMRI), has been the mainstay of noninvasive brain function imaging[1,2]. A state-of-the-art 7 Tesla (7 T) MRI system can achieve a sub-millimeter/sub-second spatiotemporal resolution but weighs over 20 tons and costs more than six million dollars[3,4]. Moreover, MRI is contraindicated in some patients with ferromagnetic implants or claustrophobia and can be difficult to tolerate due to the loud operation noise[5,6]. Alternatively, nuclear-based neuroimaging approaches can image neurometabolism, but they generally have poor temporal resolutions and are limited by the use of radioactive isotopes[7]. Electroencephalography (EEG), magnetoencephalogram (MEG), and functional near-infrared spectroscopy (fNIRS) can provide high temporal resolutions but suffer from poor spatial resolutions and lack anatomical information[8,9]. While functional ultrasound (fUS) has been demonstrated in human neonatal brains through fontanelles, it is limited to a relatively small coronal field of view (FOV) and insensitive to blood flows parallel to the probe surface due to the angle dependence of the Doppler effect[10].

Photoacoustic (PA) computed tomography (PACT) reconstructs the vasculature noninvasively using acoustic waves stemming from the optical absorption of endogenous hemoglobin (Hb) and thus can image neuroactivities based on neurovascular coupling[11]. In contrast to BOLD fMRI, PACT is directly sensitive to both deoxyhemoglobin (HbR) and oxyhemoglobin (HbO_2). The linear relationship of their distinct spectral signatures allows quantification of both concentrations and conversion to oxygen saturation (sO_2) and cerebral blood volume (CBV)[12]. In the last two decades, PACT has been explored in angiology, oncology, gastroenterology, cardiology, and neurology[11–21]. However, PACT of the human brain has not been achieved yet. Previously described panoramic 2D PACT systems could not discriminate between signals originating from the brain versus overlying tissues due to the lack of elevational resolution[11,22]. Additionally, previously described 3D systems were either too slow to overcome motion artifacts and capture fast functional signals or insufficiently sensitive to detect subtle hemodynamic changes[23–26]. Here we

report *in vivo* 3D functional human brain PACT system of 1024 (1K) parallel ultrasonic transducer elements, termed 1K3D-fPACT. Functional imaging was performed in post-hemicraniectomy patients by replicating landmark fMRI tasks of motor and language. The recorded functional activation was validated against 7 T fMRI results and self-verified by repeated measurements. We also imaged a patient with metal implants and demonstrated the 1K3D-fPACT in populations in whom MRI was not well tolerated. Collectively, in its infancy the proposed technology demonstrates comparable results to the current gold standard for imaging human brain vasculature and function.

Results

1K3D-fPACT system.

The design of the 1K3D-fPACT centers around the challenges associated with FOV, sensitivity, spatiotemporal resolution, functional contrast, ergonomic head support, and motion control. As shown in Fig. 1a,b, the 1K3D-fPACT consists of five main parts: a dual-wavelength (1064 nm and 694 nm) laser module to excite PA waves with both HbO_2 and HbR contrasts, four 256-element quarter-ring ultrasonic transducer arrays evenly distributed on a hemispherical bowl to record PA signals panoramically, a one-to-one mapped signal amplification and data acquisition (DAQ) system to amplify and digitize the PA signals, a scanning mechanism to provide azimuthal samplings, and a head support and a height-adjustable bed to stabilize the head ergonomically. See Methods for system design and construction details. The system schematic and infrastructure are shown in Supplementary Figs. 1 and 2. The 1K3D-fPACT is operated via in-house developed software that enables dual scanning modes—baseline and function. Measurement starts with the baseline mode to acquire brain angiography followed by the functional mode to image brain function. The data acquisition and laser control methodologies are detailed in Methods and Supplementary Fig. 3. Currently, the 1K3D-fPACT provides a 10-cm–diameter FOV on the head, an isotropic spatial resolution of 350 μm, and a temporal resolution of 10 s for the baseline mode and 2 s for the functional mode. However, the 1K3D-fPACT is scalable in terms of imaging rate and FOV (see Methods). The >20,000 (at 1064 nm) and >2,000 (at 694 nm) detector positions distributed on a hemisphere formed by each one-way functional scan allows the system to retain detectability of ~2% Hb signal change for 1064 nm and ~6% Hb signal change for 694 nm up to ~11 mm below the cortical surface or ~20 mm from the skin surface—deep enough to image the entire cortical thickness of the cerebral gyri[27]. See Supplementary Fig. 4 for the characteristics of the system performance.

Brain angiography.

Empowered with a high spatiotemporal resolution and sensitivity, the 1K3D-fPACT can image both brain function and angiographic structures, facilitating the co-registration between fPACT and fMRI results. Brain angiography was performed in four post-hemicraniectomy subjects using both the 1K3D-fPACT and 7 T magnetic resonance angiography (MRA) (see Methods for subjects). Considering the larger absorption coefficient of HbO_2 at 1064 nm, the baseline images acquired at 1064 nm were used to evaluate the PACT angiography. The MRA was acquired using a time-of-flight (TOF) sequence that provided an isotropic spatial resolution of 0.4 mm (see Methods). For

comparison, the 3D MRA and PACT images were first segmented into scalp and cortical regions based on the cortical contours. The MRA images were then truncated to preserve all vessels within 4 cm of the scalp surface. The segmented scalp and cortical vasculatures were individually co-registered (Supplementary Fig. 5) and presented as maximum amplitude projections (MAPs) in Fig. 2a–d. The 1K3D-fPACT angiography and MRA result in a strong visuospatial correlation (Supplementary Videos 1 and 2). Vessel pattern discrepancies are attributable to two reasons. First, the MRA TOF sequence detects inflow effects, which are only sensitive to arteries. In comparison, PACT is sensitive to Hb and images both arteries and veins. Second, since PACT and MRA were conducted non-concurrently and in different subject positions (lateral decubitus versus supine), spatial discrepancies could arise from tissue deformation, exacerbated by the craniectomy, and errors in spatial co-registration between modalities. Quantitively, the measured vasculature diameters of Subject 1 exhibit a strong agreement (Fig. 2e). Although we used the angiographic results mainly for co-registration and comparisons, the potential of the 1K3D-fPACT to diagnose cerebral vascular diseases is evident.

Mapping motor function.

Three block-designed motor tasks—sequential finger tapping (FT), lip puckering (LP), and tongue tapping (TT), were imaged using the 1K3D-fPACT and 7 T fMRI (see Methods for protocols, Supplementary Fig. 6 for stimulation paradigms, and Supplementary Video 3 for the experimental video). Functional responses to these tasks have been demonstrated to involve anatomically proximate cortical regions that require a high spatial resolution to differentiate[28]. For both modalities, brain activities were extracted for each voxel based on its absolute value fluctuation using the general linear model (GLM) (see Methods and Supplementary Methods 1)[29]. The functional maps were registered to the T1-weighted cortical images based on a systematic co-registration framework (Supplementary Fig. 5) and presented in Fig. 3a–h. See Supplementary Videos 1 and 2 for comparisons of results between modalities. The goodness of fit of the GLM was examined using *F*-test (Supplementary Fig. 7). In Fig. 3i–p, the spatial correspondence between the *t*-maps was assessed using three metrics—dice coefficient (DC), spatial correlation (SC), and center-of-mass error (CE) (see Methods). The DCs ranged from 0.30 to 0.56 for all motor tasks resulting in a fair to moderate agreement. The SCs ranged from 0.29 to 0.47 for all motor tasks resulting in a fair to moderate agreement. The CEs ranged from 0.54 to 12.86 mm demonstrating acceptable CE variations except for TT. Furthermore, we repeated measurements to evaluate the result reproducibility when the subjects were repositioned on the scanner in separate sessions (Supplementary Fig. 8 and Supplementary Tables 1 and 2). Receiver operating characteristic (ROC) curves were generated based on the data of motor tasks. For each task, the fPACT results of the same task were used as the positive samples, and the fPACT results of the other two tasks were used as the negative samples. fMRI results were used as the gold standards, and SC was chosen as the metric because it was independent of *t*-scores thresholding. The ROCs were produced by varying the threshold of SC from –1 to 1. Figure 3q shows the ROC averaged across motor tasks at each threshold value. A threshold within (0.13, 0.27) produced a sensitivity (true positive rate) of 83% and specificity (1–false positive rate) of 85%–93% (solid red line). The average area under ROC (AUC) was calculated to be 0.94.

We used the FT data as representatives for temporal analysis (Supplementary Fig. 9a,b). Figure 3r shows the mean fractional changes of BOLD and PA signals over stimulation cycles averaged across subjects. The concentration fractional changes of Hb species are shown in Fig. 3s (Supplementary Methods 2). The total Hb (HbT) concentration changes also reflect the local blood volume changes as they are proportional. Since the reciprocal of BOLD signals acquired with gradient echo had been demonstrated to correlate well with HbR, we used 1/BOLD to correlate with the concentration fractional changes of Hb species and observed a strong correlation (Fig. 3t)[30]. As the optical absorptions of HbO_2 and HbR are dominant at 1064 nm and 694 nm, respectively, the fractional changes of 1/BOLD and PA signals also establish a strong correlation ($r = 0.89$ for 1064 nm and $r = 0.96$ for 694 nm) (Supplementary Fig. 9c). Figure 3u shows the relative changes of sO_2 averaged across subjects demonstrating a ~1% sO_2 relative change. Repeated measurements in separate sessions show reproducible temporal responses (Supplementary Fig. 10). We compared the response speeds of BOLD and PACT-derived signals in response to stimulations. The onset time, defined as time to 50% peak (> two SEM at $t = 0$; SEM, standard error of the mean), was found to be 7.8 ± 0.6 s for BOLD, 6.5 ± 0.6 s for sO_2, and 6.1 ± 0.7 s for HbT (mean ± SD, $n = 4$ subjects), demonstrating that the 1K3D-fPACT can detect function faster than BOLD fMRI ($p = 0.039$ for BOLD and sO_2, $p = 0.022$ for BOLD and HbT, paired one-sided Student's t-test) due to its diverse functional contrasts (Supplementary Fig. 9d). We define the contrast-to-noise ratio (CNR) of the functional signals as $CNR = S / SEM$, where S is the mean of the absolute contrasts between the signal peaks and the baselines over stimulation cycles. Figure 3v shows that the average CNR of the PA signals at 1064 nm is lower but comparable to that of BOLD signals. Due to fewer scanning angles, the CNR of the PA signals acquired at 694 nm is relatively lower yet has an average value greater than two.

Mapping language areas.

To evaluate the 1K3D-fPACT for mapping different aspects of language-evoked brain function, we used passive story listening (PL) and silent word generation (WG) tasks to isolate the sensory and semantic aspects of language function (see Methods for protocols and Supplementary Fig. 6 for stimulation paradigms). In Fig. 4, functional maps from fPACT and fMRI were extracted and co-registered to the T1-weighted cortex following the same data processing routines (Supplementary Methods 1). For both fMRI and fPACT, the WG results show a relatively broad area of activation, which corresponds grossly to Broca's area. Broca's area is predominantly located in the left hemisphere[31], and our results are consistent with this fact given that results from Subjects 1 and 2 demonstrated strong activation, while Subject 3's right hemisphere showed less significant activation (to be shown in Fig. 5d). See Supplementary Videos 1 and 2 for cross-modality comparisons of the functional results. The DCs of 0.41 and 0.50, and SCs of 0.33 and 0.51 result in a fair to a moderate agreement for PL. The smaller DCs for WG are most likely attributable to the thresholding-induced discontinuity in the activated clusters, because the SCs implicate a better agreement. The CEs range from 4.87 mm to 7.00 mm demonstrating acceptable localization discrepancies. Repeated measurements also demonstrate good repeatability of the functional results (Supplementary Fig. 8 and Supplementary Tables 1 and 2).

Mapping brain function in a subject with implants.

Subject 3 required metal implants for the treatment of an orthopedic injury sustained in conjunction with the head trauma. The implants were cleared for 7 T; however, discomfort at the implant site during fMRI acquisition was significant enough to require abortion of the scan. Consequently, only T1-weighted MRI, MRA, and fMRI of FT were acquired. Implants are not uncommon in craniectomized patients due to the polytraumatic nature of many traumatic brain injuries (e.g., implanting fixation plates at fracture sites). Due to the non-invasive and magnet-free nature of the 1K3D-fPACT, all functional studies were attained in Subject 3 without reported issues. Although without the fMRI results, the functional responses to LP, TT, and PL recorded by the 1K3D-fPACT exhibit topographies comparable to those obtained in the other subjects (Figs. 3 and 4) and the reported results[32,33]. In Fig. 5d, the less significant and non-reproducible responses to WG are attributable to the fact that the right hemisphere is not the dominant hemisphere for language (Supplementary Fig. 8 and Supplementary Table 2)[31]. In contrast, the fMRI and fPACT results of Subjects 1 and 2 showed significant responses in the left hemispheres as indicated in Fig. 4d,e, and repeated measurements in Supplementary Fig. 8a,b. Therefore, the WG data of Subject 3 (Fig. 5d and repeated measurements in supplementary Fig. 8c) can be considered a negative control. The anatomic and functional results of Subject 3 are displayed in Supplementary Video 2.

Discussion and outlook

This study demonstrated PACT technology in imaging human brain function. We employed motor tasks to evaluate the 1K3D-fPACT capability to discriminate between anatomically proximate areas, and the language protocols to image distributed brain activities. The functional results demonstrate a ~1-cm depth from the cortical surface and are quantitively comparable to those obtained with 7 T fMRI. Discrepancies are attributable to the following factors. First, experiments of fPACT and fMRI were non-concurrent, leading to physiological variations. Second, tissue deformation induced by different imaging postures of the two modalities introduced co-registration errors. Third, although it is the current gold standard, fMRI still has limitations regarding sensitivity and specificity for functional imaging.

In this study, the radiant exposure on the skin was ~23 mJ/cm^2 for 1064 nm, approximately 1/4 the ANSI limit (100 mJ/cm^2, see Methods)[34]. If the radiant exposure is increased to the ANSI limit, we expect to detect function at a greater depth of ~2.3 cm where the current detectability is ~8% (Supplementary Fig. 4c). Compared with MRI, the 1K3D-fPACT is currently limited to imaging the superficial cortex. However, it can potentially monitor the resting-state dynamics in at least portions of all the major networks through their nodes in the cortex[35].

Although the unique hemicraniectomy population provides an acoustic window allowing for aberration-free image reconstruction, transcranial PACT is potentially achievable. For transcranial PACT, the signal-to-noise ratio (SNR) is compromised by the skull-induced optical attenuation and acoustic aberration (including acoustic attenuation and wavefront distortion). Our preliminary studies have shown that an adult human skull induces ~50% light attenuation at 1064 nm and ~80% acoustic pressure attenuation[36]. Given the SNR of

~50 achieved at ~11 mm below the cortical surface in hemicraniectomy patients, the SNR for transcranial PACT at the same cortical depth would decrease to ~5. In order to detect the functional change of typically several percent, further improvement is required. First, a system with a lower center frequency (e.g., 1 MHz) is desired because the skull-induced acoustic attenuation is frequency-dependent, and the transcranial PA signal centers at ~0.75 MHz[36]. Since the dimension of an ultrasonic transducer element is inversely proportional to its center frequency for a given acceptance angle, the dimension of a 1-MHz transducer element should be 2.1 times that of the current system, improving the SNR by 2.1 times. Second, if the radiant exposure is increased to the ANSI limit, the SNR can be improved by a factor of ~4. Third, given that the current element count can be tripled, the SNR can gain another factor of $\sqrt{3}$. With the above potential improvement, we expect the transcranial detectability to be ~1.4% at ~1 cm below the cortical surface. The recent improvement in ultrasonic transducer sensitivity can also potentially enhance the SNR of transcranial PACT[37]. However, one should note that the estimated SNR above assumed no skull-induced acoustic distortion. State-of-the-art de-aberration techniques are mainly based on full-wave acoustic modeling and the assumption of homogeneous skull acoustic properties. The current challenges are high computational cost and limited reconstruction quality[38–41]. We are developing the next-generation reconstruction algorithms that account for the skull acoustic heterogeneity and incorporate artificial intelligence (AI) for speed[42–44].

Table 1 includes relevant comparisons between the 1K3D-fPACT and BOLD fMRI in functional human brain imaging. Fundamentally, the 1K3D-fPACT can quantify the concentrations of both HbO_2 and HbR. Other contrasts, including sO_2 and cerebral blood volume (CBV), can be derived from HbO_2 and HbR concentrations. The diverse contrasts of the 1K3D-fPACT allow it to detect functional activation faster than BOLD fMRI: 6.1 ± 0.7 s versus 7.8 ± 0.6 s (mean ± SD, n = 4 subjects), and potentially with greater specificity. As the system performance evolves, we expect to detect even faster functional activation as demonstrated in small animals[45]. At certain near-infrared wavelengths, PA signals are almost exclusively from Hb species due to their much higher absorption coefficients than other tissue components. This results in excellent sensitivity in detecting Hb with negligible background. In contrast, BOLD fMRI detects neural activities based on only paramagnetic HbR in a nonlinear relationship with a modest sensitivity due to substantial tissue background. Practically, the 1K3D-fPACT has benefits over MRI in portability, space, operation sound, operation and maintenance costs. Free of strong magnetic fields, the 1K3D-fPACT is also able to obtain functional images in patients with ferromagnetic implants/devices. Similarly, the 1K3D-fPACT will be favorable for introducing neuromodulators and complementary imaging/recording modalities, creating unique clinical and research opportunities. Collectively, the presented results demonstrate that fPACT technology is likely to be a robust, powerful, and practical tool for human neuroimaging in the future.

Methods

1K3D-fPACT system design and construction.

To enrich the functional contrast, two types of Q-switched laser, Nd:YAG (pulse repetition frequency (PRF): 10 Hz, maximum pulse energy: ~2.2 J, pulse width: 8–12 ns) and ruby

(PRF: 1 Hz, maximum pulse energy: ~1.7 J, pulse width: 12–20 ns), are used to enable dual-wavelength contrasts at HbO_2 dominant 1064 nm and HbR dominant 694 nm. To improve the sensitivity and spatiotemporal resolution, a massively parallel 1024-element ultrasonic transducer array was lab-designed and custom-built with a 1.5×1.5 mm^2 active element area, 2.4-mm element pitch distance, and 2.12-MHz central frequency with a one-way –6-dB bandwidth (BW) of 1.73 MHz and a one-way fractional bandwidth (FBW) of 78% (Supplementary Fig. 4a). The 1024 elements are evenly distributed in four-quarter rings directly connected to four 256-channel ultra-low-noise pre-amplifier modules (51-dB gain). The amplified PA signals are digitized by four 256-channel DAQ boards (12-bit dynamic range, 20-MHz sampling rate, 6-dB gain, 7.5-MHz analog anti-aliasing filter) and streamed to a workstation via USB 3.0 in real time. The four-quarter-ring design allows not only sufficiently dense elevational samplings but also an anatomical scan (400 azimuthal scanning angles) to be completed within a 10-s single-breath-hold period and a functional volumetric imaging rate of 0.5 Hz (80 azimuthal scanning angles at 1064 nm and 8 azimuthal scanning angles at 694 nm). We chose a customized hemispherical array instead of a commercially available matrix array because the hemispherical configuration offers a panoramic view of the object, providing a larger FOV with a nearly isotropic 3D resolution and significantly reduced limited-view artifacts[46,47]. We preferred one-to-one mapped pre-amplifiers and DAQs to multiplexing because multiplexing electronics limit data throughput and may introduce noise and crosstalk. The four-quarter rings were manufactured on the inner surface of a 26-cm–diameter polytetrafluoroethylene (PTFE) hemispherical bowl that can both hold the acoustic coupling medium and reflect/recycle the scattered/reflected excitation light. Considering that deuterium oxide (D_2O) has a light absorption coefficient (0.01 cm^{-1}) ten times smaller than that of ordinary water at 1064 nm (0.1 cm^{-1}) and a similar one (0.006 cm^{-1}) at 694 nm, we use D_2O (sterilized and recycled) as the acoustic coupling medium between the transducers and the head to maximize the light delivery[48]. The spatial resolution, in terms of full width at half maximum (FWHM) of the point spread function (PSF), was measured to be 350 μm isotropic in acoustically homogeneous D_2O (Supplementary Fig. 4b). The laser pulses are partially reflected and sampled by a photodiode to correct for energy fluctuations. An engineered diffuser installed at the bottom center of the bowl transducer is used to homogenize and expand the laser beams to ~10 cm in diameter on the head. Given the light attenuation in the light path, PRF, and illumination area, the radiant exposure (~23 mJ/cm^2 at 1064 nm and ~19 mJ/cm^2 at 694 nm) and fluence rate (~230 mW/cm^2 at 1064 nm, ~19 mW/cm^2 at 694 nm, and ~249 mW/cm^2 at the two wavelengths) are within the American National Standards Institute (ANSI) safety limits (100 mJ/cm^2 and 1000 mW/cm^2 at 1064 nm, 20 mJ/cm^2 and 200 mW/cm^2 at 694 nm, and 860 mW/cm^2 at the two wavelengths)[34]. As designed, the system adopts supine, lateral, and prone positions as standard imaging postures. A height-adjustable bed is used to adjust the trunk height relative to the imager for ergonomic comfort. Although the imaging postures optimized the tradeoff between comfort and stability, maintaining a stable head position during functional tasks, with acquisition times of approximately 10 minutes, posed significant challenges to the head support design. The head support was designed around a hollow PTFE panel detachable from the system. A tensioned disposable polyvinylidene chloride (PVC) film, which was acoustically and optically transparent, was mounted to the panel to support and constrain the head in the vertical direction. The film also functions as

an isolation layer to prevent cross contamination of D_2O among subjects. A small amount of distilled water is applied on top of the film to enhance the acoustic coupling between the skin and the film. To constrain the lateral motion, a press-fit head holder with closable fingers designed and custom-made was mounted to the PTFE panel. Finally, three horizontal fasteners were used to push the fingers against the head to introduce more fingers-head friction to constrain the rotational motion of the head. The resulting comfort level enabled imaging sessions to last up to two hours without reported discomfort. The schematic and infrastructure of the 1K3D-fPACT system are shown in Supplementary Figs. 1 and 2.

1K3D-fPACT acquisition.

The transducer array was rotated 90 degrees in 100 equiangular steps reciprocally to simultaneously acquire ten densely sampled images at 1064 nm and ten partially sampled images at 694 nm in 108 s. The laser interleaving scheme is described in Supplementary Fig. 3. To achieve an equal spatial sampling density to that of the 1064-nm images, the 694-nm images were merged after correcting for their relative shifts based on co-registration of the ten 1064-nm images. The functional scan was performed by rotating the array reciprocally over 90 degrees at 0.5 Hz resulting in a temporal resolution of 2 s. In each one-way scan, there were 20 equiangular acquisition steps for 1064 nm and two equiangular acquisition steps for 694 nm. The functional volumetric images were reconstructed using the baseline images as constraints to improve the image SNR and reduce the streaking artifacts induced by limited scanning angles (Supplementary Methods 1).

Scalability of the 1K3D-fPACT.

The 1K3D-fPACT is scalable in terms of imaging rate and FOV. The current functional scan is configured to 0.5 Hz to balance the spatial sampling density and imaging rate. However, it can be improved by using high-PRF lasers, combining multiple laser sources/increasing the transducer element count. The current FOV (~10 cm in diameter on the head) is limited by the illumination area (proportional to the laser pulse energy with radiant exposure kept constant) and sampling density (proportional to the laser PRF and transducer element count for the same imaging rate). Therefore, improving the laser PRF or element count can enlarge the FOV. However, one should note that there is an upper limit for the laser RPF defined by the ANSI safety standards detailed in Methods. The PA amplitude is proportional to the radiant exposure, and thus the highest radiant exposure, within the safety limit, provides the highest SNR if the image acquisition time is held constant.

7 T MRI acquisition.

MRI was collected using a 7 T Siemens Terra scanner (Siemens Medical Solutions USA, Inc.) and a Nova Medical 32-channel head coil (Siemens Medical Solutions USA, Inc.). The T1-weighted anatomical image was first collected using the Magnetization Prepared Rapid Gradient Echo (MPRAGE) (echo time (TE) = 2.95 ms, repetition time (TR) = 2,200 ms, flip angle (FA) = 7°, 0.7×0.7×0.7 mm^3 isotropic voxel, FOV = 224 mm, matrix = 320×320, 240 slices). Subsequently, a TOF-MRA (TE = 4.67 ms, TR = 12 ms, FA = 20°, 0.4×0.4×0.4 mm^3 isotropic voxel, 4 slabs, slices per slab = 60 transverse, FOV = 200 mm, matrix = 496×496) was acquired. The BOLD fMRI was obtained using a multiband (MB) gradient-echo EPI sequence (TE = 22 ms, TR = 3,000 ms, FA = 80°, phase acceleration

factor = 5, simultaneous multi-slice = 2, 1.0×1.0×1.0 mm^3 isotropic voxel, FOV = 192 mm, matrix = 192×192, 92 slices). The fMRI data were pretreated with motion correction, spatial smoothing (3-mm FWHM Gaussian kernel, consistent with the fPACT data), and temporal filtration (0.01-Hz high pass, fourth-order Butterworth) before being analyzed by the GLM in SPM12[49].

1K3D-fPACT validation with 7 T fMRI.

The functional results from both modalities were quantitively compared using DC, SC, and CE. The DC measures the normalized intersection between two functional maps using $2(A_{fPACT} \cap A_{fMRI})/(A_{fPACT}+A_{fMRI})$, where A_{fPACT} and A_{fMRI} are the areas of activated regions of interest (ROI) in fPACT and fMRI results. The SC evaluates the spatial correspondence without thresholding. The CE characterizes the localization discrepancies by calculating the absolute Euclidian distance between the weighted centers of mass of the activated ROI in fPACT and fMRI results. The DC and SC results are classified as "no agreement" for [–1, 0], "slight agreement" for (0 0.2), "fair agreement" for [0.2, 0.4), "moderate agreement" for [0.4, 0.6), "substantial agreement" for [0.6, 0.8), and "almost perfect agreement" for [0.8, 1][50].

Subjects.

The study was approved by the institutional review boards of the California Institute of Technology (Caltech), the University of Southern California (USC), and the Rancho Los Amigos National Rehabilitation Center (RLA). Four adult male post-hemicraniectomy patients (Subject 1: left hemicraniectomy, aged 34, not Hispanic or Latino; Subject 2: left hemicraniectomy, aged 25, Latino; Subject 3: right hemicraniectomy, aged 19, not Hispanic or Latino; Subject 4: right hemicraniectomy, aged 41, Latino) with clinically intact neurologic exams and completely healed surgical wounds were recruited from RLA. PACT was performed at Caltech, and MRI was conducted at USC. All subjects had to pass 7 T screening to ensure safe participation. All subjects agreed to shave their head for efficient light delivery in the PACT sessions. Written informed consent was obtained from all subjects according to the study protocols. Subjects 1, 3, and 4 underwent multiple fPACT sessions to assess the reproducibility of the fPACT results. As a well-established modality, MRI was acquired only once non-concurrently but on the same day with the first PACT session. Subject 3 dropped out of the fMRI session after the T1-weighted MRI, MRA, and FT fMRI being obtained. Subject 2 underwent FT in both modalities and PL only in fPACT because of hearing difficulties in the MRI scanner. Subject 2 had difficulties in performing the other tasks. The authors affirm that human research participants provided written informed consent for publication of the retinal images and potentially identifiable information in Fig. 2 and Video 3 of the supplementary information and the 'Subjects' section of the manuscript.

Protocols.

For fPACT stimuli, a subject lay on a height-adjustable bed with two stereo speakers placed on both sides of the head. During fMRI, stimuli were presented via a 7 T compatible earphone system (S15, Sensimetrics, Corp.). Both fPACT and fMRI shared the same auditory cues. The auditory cues used a short rising tone beep as the start of a stimulus

and a falling tone beep as the end. Subjects were pre-trained and imaged with one or more of the following stimuli: FT, LP, TT, LP, and WG. Stimulation paradigms can be found in Supplementary Fig. 6.

Supplementary Material

Refer to Web version on PubMed Central for supplementary material.

Acknowledgements

The authors thank Miss Guadalupe Corral-Leyva for patient care and Yilin Luo for discussion on the potential of AI in advancing PACT. This work was sponsored by the United States National Institutes of Health (NIH) grants R35 CA220436 (Outstanding Investigator Award), U01 NS099717 (BRAIN Initiative), R01 NS102213, R01 NS114382, R01 EB028297, and Caltech internal funds (PPF0021).

Data availability

The data that support the findings of this study are provided in the main text and Supplementary Information. 3D functional image stacks of fMRI and fPACT for Subject 3 FT and LP session 1 are available at https://doi.org/10.5061/dryad.sxksn0310. Other data are too large to be publicly shared, yet they are available for research purposes from the corresponding authors on reasonable request.

References

1. Logothetis NK What we can do and what we cannot do with fMRI. Nature 453, 869–878 (2008). [PubMed: 18548064]
2. Ogawa S, Lee T-M, Kay AR & Tank DW Brain magnetic resonance imaging with contrast dependent on blood oxygenation. Proc. Natl. Acad. Sci 87, 9868–9872 (1990). [PubMed: 2124706]
3. Pfeuffer J et al. Zoomed functional imaging in the human brain at 7 Tesla with simultaneous high spatial and high temporal resolution. Neuroimage 17, 272–286 (2002). [PubMed: 12482083]
4. Nowogrodzki A The world's strongest MRI machines are pushing human imaging to new limits. Nature 563, 24–26 (2018). [PubMed: 30382222]
5. Schenck JF The role of magnetic susceptibility in magnetic resonance imaging: MRI magnetic compatibility of the first and second kinds. Med. Phys 23, 815–850 (1996). [PubMed: 8798169]
6. Price DL, De Wilde JP, Papadaki AM, Curran JS & Kitney RI Investigation of acoustic noise on 15 MRI scanners from 0.2 T to 3 T. J. Magn. Reson. Imaging Off. J. Int. Soc. Magn. Reson. Med 13, 288–293 (2001).
7. Rahmim A & Zaidi H PET versus SPECT: strengths, limitations and challenges. Nucl. Med. Commun 29, 193–207 (2008). [PubMed: 18349789]
8. Darvas F, Pantazis D, Kucukaltun-Yildirim E & Leahy RM Mapping human brain function with MEG and EEG: methods and validation. NeuroImage 23, S289–S299 (2004). [PubMed: 15501098]
9. Eggebrecht AT et al. Mapping distributed brain function and networks with diffuse optical tomography. Nat. Photonics 8, 448 (2014). [PubMed: 25083161]
10. Demene C et al. Functional ultrasound imaging of brain activity in human newborns. Sci. Transl. Med 9, eaah6756 (2017). [PubMed: 29021168]
11. Wang X et al. Noninvasive laser-induced photoacoustic tomography for structural and functional in vivo imaging of the brain. Nat. Biotechnol 21, 803–806 (2003). [PubMed: 12808463]
12. Wang LV & Hu S Photoacoustic tomography: in vivo imaging from organelles to organs. science 335, 1458–1462 (2012). [PubMed: 22442475]

13. Li L et al. Single-impulse panoramic photoacoustic computed tomography of small-animal whole-body dynamics at high spatiotemporal resolution. Nat. Biomed. Eng 1, 0071 (2017). [PubMed: 29333331]
14. Wray P, Lin L, Hu P & Wang LV Photoacoustic computed tomography of human extremities. J. Biomed. Opt 24, 026003 (2019).
15. Lin L et al. Single-breath-hold photoacoustic computed tomography of the breast. Nat. Commun 9, 1–9 (2018). [PubMed: 29317637]
16. Jathoul AP et al. Deep in vivo photoacoustic imaging of mammalian tissues using a tyrosinase-based genetic reporter. Nat. Photonics 9, 239–246 (2015).
17. Wu Z et al. A microrobotic system guided by photoacoustic computed tomography for targeted navigation in intestines in vivo. Sci. Robot 4, eaax0613 (2019). [PubMed: 32632399]
18. Lin H-CA et al. Ultrafast volumetric optoacoustic imaging of whole isolated beating mouse heart. Sci. Rep 8, 14132 (2018). [PubMed: 30237560]
19. Nasiriavanaki M et al. High-resolution photoacoustic tomography of resting-state functional connectivity in the mouse brain. Proc. Natl. Acad. Sci 111, 21 (2014). [PubMed: 24367107]
20. Gottschalk S et al. Rapid volumetric optoacoustic imaging of neural dynamics across the mouse brain. Nat. Biomed. Eng 3, 392–401 (2019). [PubMed: 30992553]
21. Ravina K et al. Prospects of Photo-and Thermoacoustic Imaging in Neurosurgery. Neurosurgery 87, 11–24 (2020). [PubMed: 31620798]
22. Nie L et al. Photoacoustic tomography through a whole adult human skull with a photon recycler. J. Biomed. Opt 17, 110506 (2012). [PubMed: 23123972]
23. Xiang L, Wang B, Ji L & Jiang H 4-D photoacoustic tomography. Sci. Rep 3, 1113 (2013). [PubMed: 23346370]
24. Deán-Ben XL et al. Functional optoacoustic neuro-tomography for scalable whole-brain monitoring of calcium indicators. Light Sci. Appl 5, e16201–e16201 (2016). [PubMed: 30167137]
25. Deán-Ben XL, Fehm TF, Ford SJ, Gottschalk S & Razansky D Spiral volumetric optoacoustic tomography visualizes multi-scale dynamics in mice. Light Sci. Appl 6, e16247–e16247 (2017). [PubMed: 30167242]
26. Matsumoto Y et al. Visualising peripheral arterioles and venules through high-resolution and large-area photoacoustic imaging. Sci. Rep 8, 1–11 (2018). [PubMed: 29311619]
27. Fischl B & Dale AM Measuring the thickness of the human cerebral cortex from magnetic resonance images. Proc. Natl. Acad. Sci 97, 11050 (2000). [PubMed: 10984517]
28. Kern M, Bert S, Glanz O, Schulze-Bonhage A & Ball T Human motor cortex relies on sparse and action-specific activation during laughing, smiling and speech production. Commun. Biol 2, 1–14 (2019). [PubMed: 30740537]
29. Friston KJ et al. Statistical parametric maps in functional imaging: a general linear approach. Hum. Brain Mapp 2, 189–210 (1994).
30. Strangman G, Culver JP, Thompson JH & Boas DA A quantitative comparison of simultaneous BOLD fMRI and NIRS recordings during functional brain activation. Neuroimage 17, 719–731 (2002). [PubMed: 12377147]
31. Pujol J, Deus J, Losilla JM & Capdevila A Cerebral lateralization of language in normal left-handed people studied by functional MRI. Neurology 52, 1038–1038 (1999). [PubMed: 10102425]
32. Brown S, Ngan E & Liotti M A larynx area in the human motor cortex. Cereb. Cortex 18, 837–845 (2008). [PubMed: 17652461]
33. Price CJ The anatomy of language: a review of 100 fMRI studies published in 2009. Ann. N. Y. Acad. Sci 1191, 62–88 (2010). [PubMed: 20392276]
34. American National Standards Institute. American National Standard for the Safe Use of Lasers ANSI z136.1–2007. (Laser Institute of America, Orlando, FL, 2007).
35. Zhang D & Raichle ME Disease and the brain's dark energy. Nat. Rev. Neurol 6, 15–28 (2010). [PubMed: 20057496]
36. Na S et al. Transcranial photoacoustic computed tomography based on a layered back-projection method. Photoacoustics 100213 (2020). [PubMed: 33134081]

37. Shnaiderman R et al. A submicrometre silicon-on-insulator resonator for ultrasound detection. Nature 585, 372–378 (2020). [PubMed: 32939068]
38. Poudel J, Na S, Wang LV & Anastasio MA Iterative image reconstruction in transcranial photoacoustic tomography based on the elastic wave equation. Phys. Med. Biol (2020).
39. Mitsuhashi K et al. A Forward-Adjoint Operator Pair Based on the Elastic Wave Equation for Use in Transcranial Photoacoustic Computed Tomography. SIAM J. Imaging Sci 10, 2022–2048 (2017). [PubMed: 29387291]
40. Javaherian A & Holman S A continuous adjoint for photo-acoustic tomography of the brain. Inverse Probl. 34, 085003 (2018).
41. Guasch L, Agudo OC, Tang M-X, Nachev P & Warner M Full-waveform inversion imaging of the human brain. NPJ Digit. Med 3, 1–12 (2020). [PubMed: 31934645]
42. Ulyanov D, Vedaldi A & Lempitsky V Deep image prior. in Proceedings of the IEEE Conference on Computer Vision and Pattern Recognition 9446–9454 (2018).
43. Heckel R & Hand P Deep decoder: Concise image representations from untrained non-convolutional networks. ArXiv Prepr. ArXiv181003982 (2018).
44. Bostan E, Heckel R, Chen M, Kellman M & Waller L Deep phase decoder: self-calibrating phase microscopy with an untrained deep neural network. Optica 7, 559–562 (2020).
45. He Y, Shi J, Maslov KI, Cao R & Wang LV Wave of single-impulse-stimulated fast initial dip in single vessels of mouse brains imaged by high-speed functional photoacoustic microscopy. J. Biomed. Opt 25, 066501 (2020).
46. Hu P, Li L, Lin L & Wang LV Spatiotemporal Antialiasing in Photoacoustic Computed Tomography. IEEE Trans. Med. Imaging (2020).
47. Xu Y, Wang LV, Ambartsoumian G & Kuchment P Reconstructions in limited-view thermoacoustic tomography. Med. Phys 31, 724–733 (2004). [PubMed: 15124989]
48. Kedenburg S, Vieweg M, Gissibl T & Giessen H Linear refractive index and absorption measurements of nonlinear optical liquids in the visible and near-infrared spectral region. Opt. Mater. Express 2, 1588–1611 (2012).
49. Ashburner J et al. SPM12 manual. Wellcome Trust Cent. Neuroimaging Lond. UK 2464 (2014).
50. Landis JR & Koch GG The measurement of observer agreement for categorical data. biometrics 159–174 (1977). [PubMed: 843571]

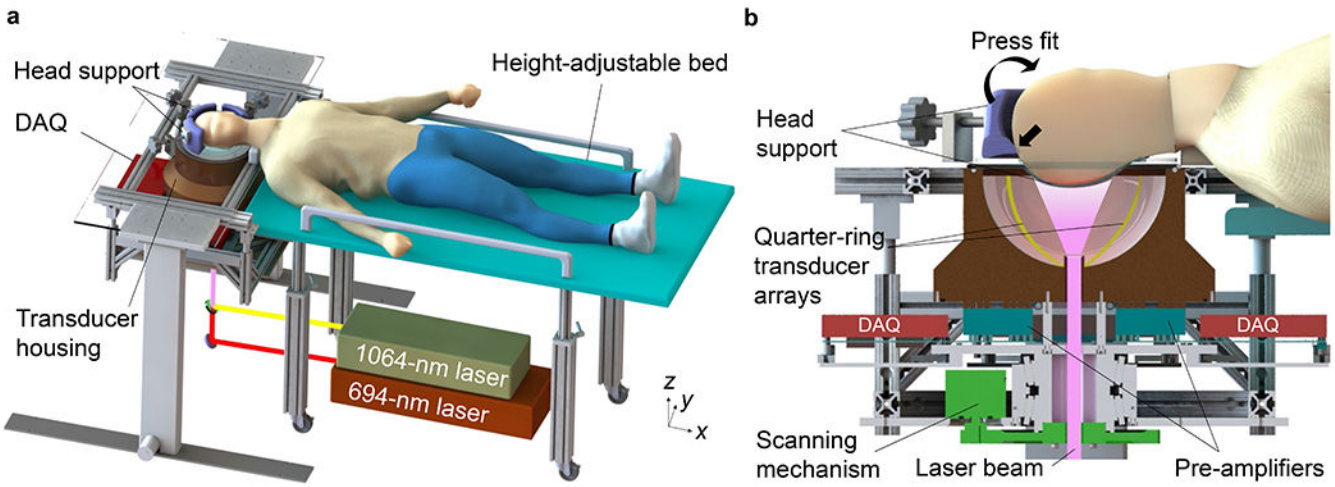

Fig. 1 |. Representations of the 1K3D-fPACT.

a, Perspective view of the system. **b**, Perspective cut-away view of the imager.

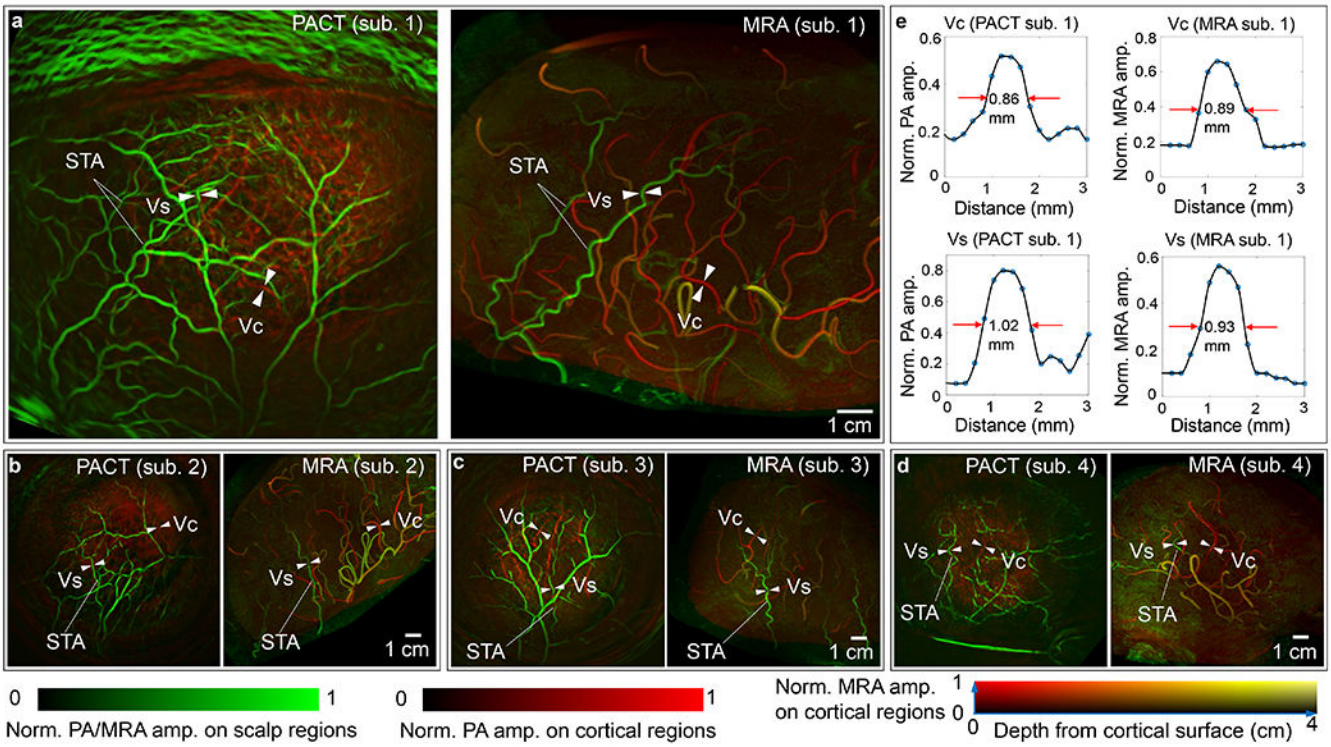

Fig. 2 |. PACT angiography and MRA of the same brains.

a–**d**, Vasculatures imaged in Subjects 1–4 using the baseline PACT (left) and MRA (right). The images were segmented into the scalp (green) and cortical (red for PACT, 2D color map for MRA) regions. The scalp and cortical images were normalized by their maximum voxel PA or MRA values (a.u.). **e**, The diameters of the selected scalp vessel (Vs) and cortical vessel (Vc) of Subject 1 were quantified as the full width at half maximum (red arrows). The *y*-axes represent the voxel amplitudes in **a**. The labeled Vs, Vc, and superficial temporal arteries (STA) in (**a**–**d**) can be referred to for visuospatial correlation. Sub., subject; norm., normalized; amp., amplitude.

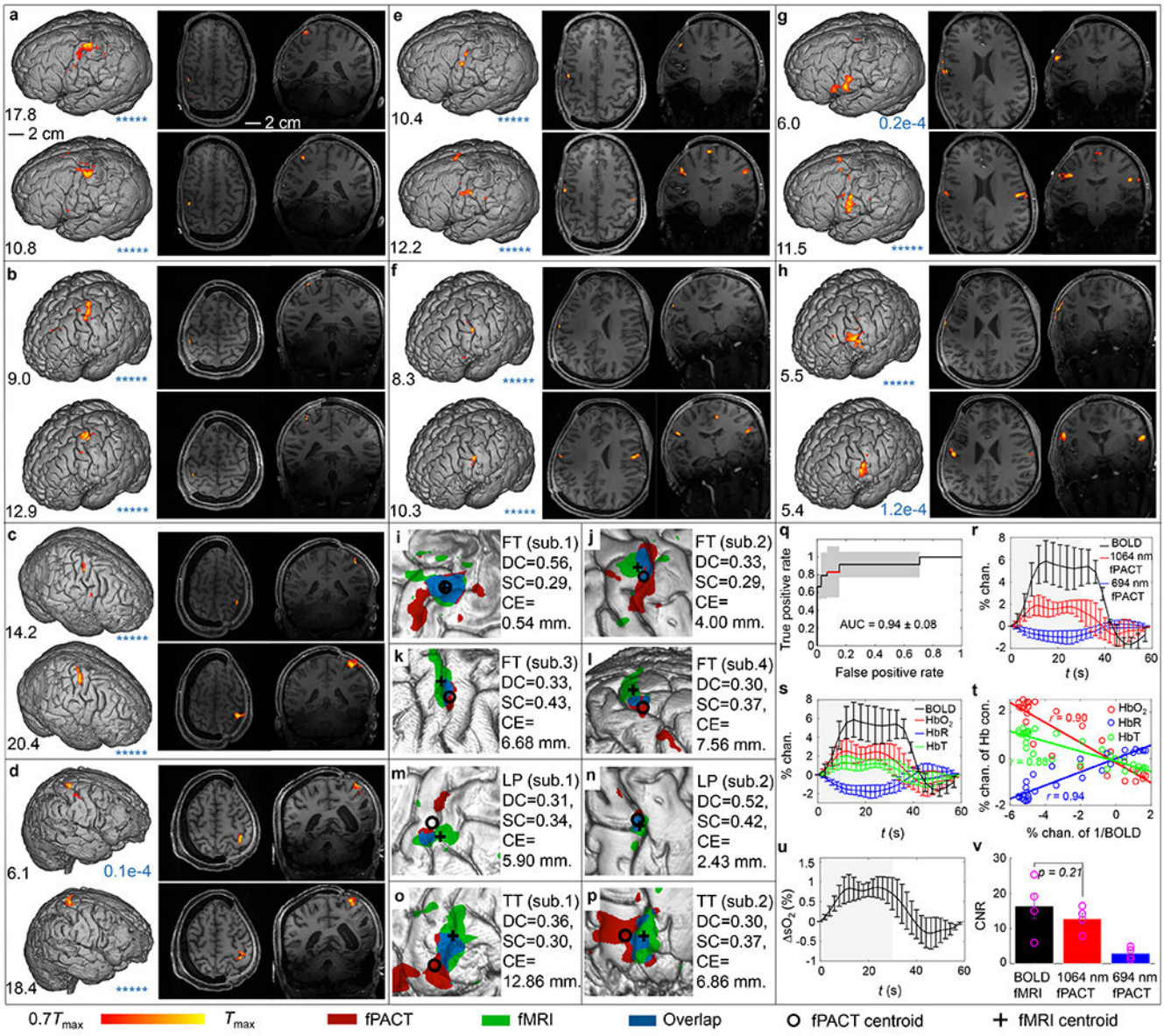

Fig. 3 |. Evaluating the 1K3D-fPACT for brain function mapping using 7 T fMRI and motor tasks.

a–**h**, Functional responses to FT were recorded in Subjects 1–4 (**a**–**d**), and responses to LP and TT were acquired in Subject 1 (**e**,**g**) and Subject 2 (**f**,**h**). The fPACT and fMRI results are displayed in the first and second rows, respectively. Each functional map reflects the *t*-values greater than 70% maximum. The maximum *t*-value (in black) is shown below the cortex. The *p*-value corresponding to 70% maximum *t*-value is displayed (in blue) below the cortex (*****$p < 0.00001$, one-sample one-sided Student's *t*-test, DOF = 222 for fPACT, DOF = 142 for fMRI, no adjustment; q (FDR) < 0.05 for all maps). The functional maps displayed on the cortex represent MAPs of the responses within a 2-cm depth. Functional distributions are displayed on the axial (middle column) and coronal (right column) brain slices that pass the midpoints of the line connecting the centroids of the activated maps of both modalities. FT, LP, and TT were measured three times for Subject 1 and once

for Subject 2; FT was measured twice for Subjects 3 and 4 (see Supplementary Fig. 8). **i**–**p**, The functional maps in the left columns of (**a**–**h**) were compared based on the DC, SC, and CE in a 4×4-cm^2 FOV. Shown are the binarized functional maps used in the DC calculation. **q**, ROC averaged across $n = 3$ motor tasks at each threshold value. Data are presented as mean ± SD. **r**, Measured fractional changes of the BOLD and PA signals during the FT task. Data are presented as mean ± SD ($n = 4$ subjects; SD, standard deviation). The gray area represents stimulation period. **s**, Calculated concentration fractional changes for each Hb species. Data are presented as mean ± SD ($n = 4$ subjects). **t**, Scatterplots of the concentration fractional changes of each Hb species vs. 1/BOLD fractional changes. **u**, The relative changes of sO_2 during FT. Data are presented as mean ± SD ($n = 4$ subjects). **v**, CNRs of BOLD and PA signals. Data are presented as mean ± SEM ($n = 4$ subjects). The *p*-value was computed using paired two-sided Student's *t*-test. Chan., change; con., concentration; *t*, time.

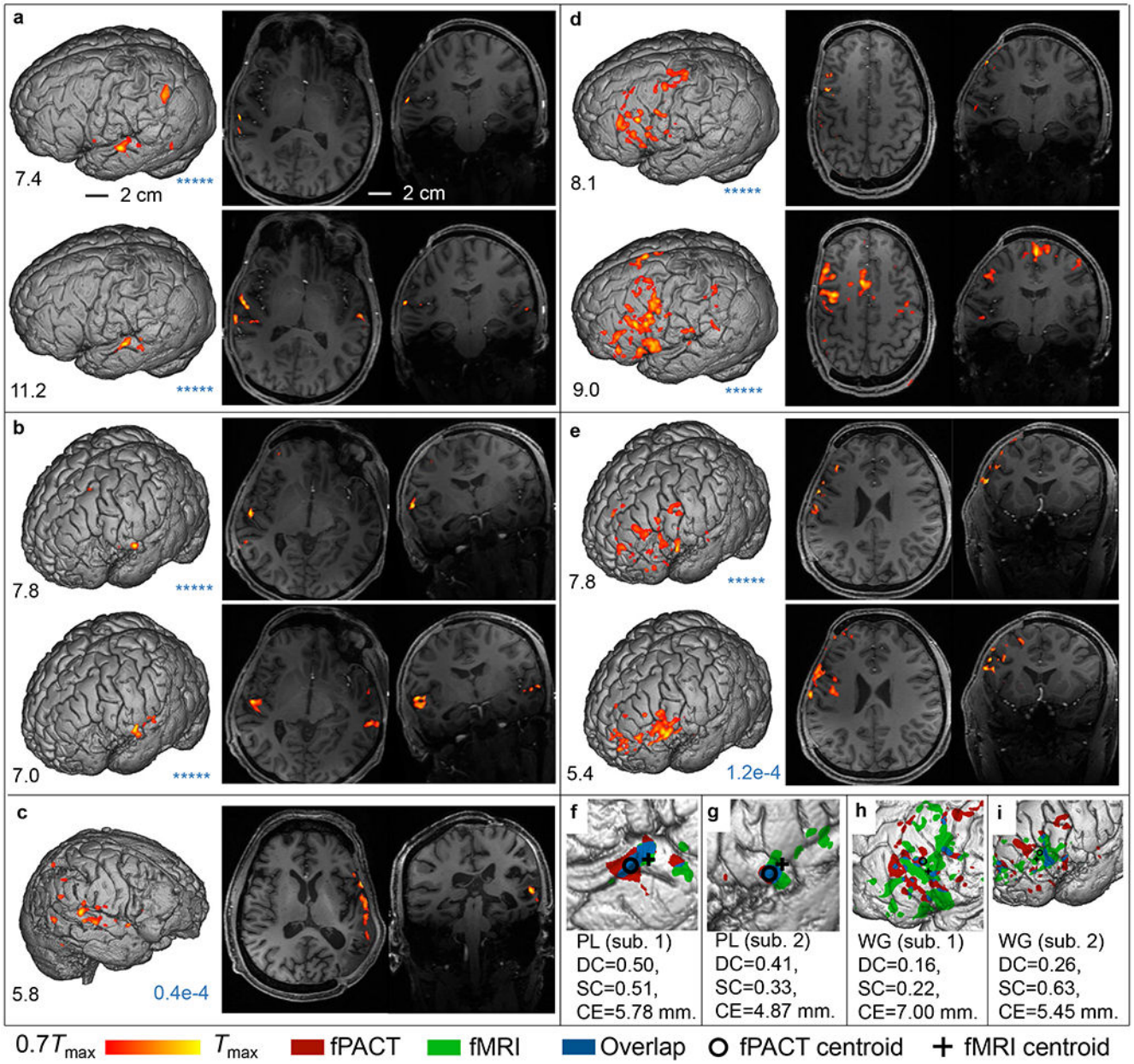

Fig. 4 |. Imaging language processing.

a–**e**, Functional responses to PL (**a**–**c**) and WG (**d**,**e**) were recorded in Subject 1 (**a**,**d**) and Subject 2 (**b**,**e**). The fPACT and fMRI results are displayed in the first and second rows, respectively. Subject 4 underwent PL only in the PACT session (**c**). The maximum *t*-value (in black) is displayed below the cortex. The *p*-value corresponding to 70% maximum *t*-value is displayed (in blue) below the cortex (*****$p < 0.00001$, one-sample one-sided Student's *t*-test, DOF = 207 for fPACT, DOF = 132 for fMRI, no adjustment; *q* (FDR) < 0.05 for all maps). PL and WG were measured three times for Subject 1 and once for Subject 2; PL was measured twice for Subject 4 (see Supplementary Fig. 8). **f–i**, The binary masks of the responses are displayed in a FOV of 4×4 cm^2 for PL (**f**,**g**) and 10×10 cm^2

for WG (**h**,**i**). For Subject 4, the PL responses fall into the auditory cortex regions, which topographically agrees with those observed in the other subjects.

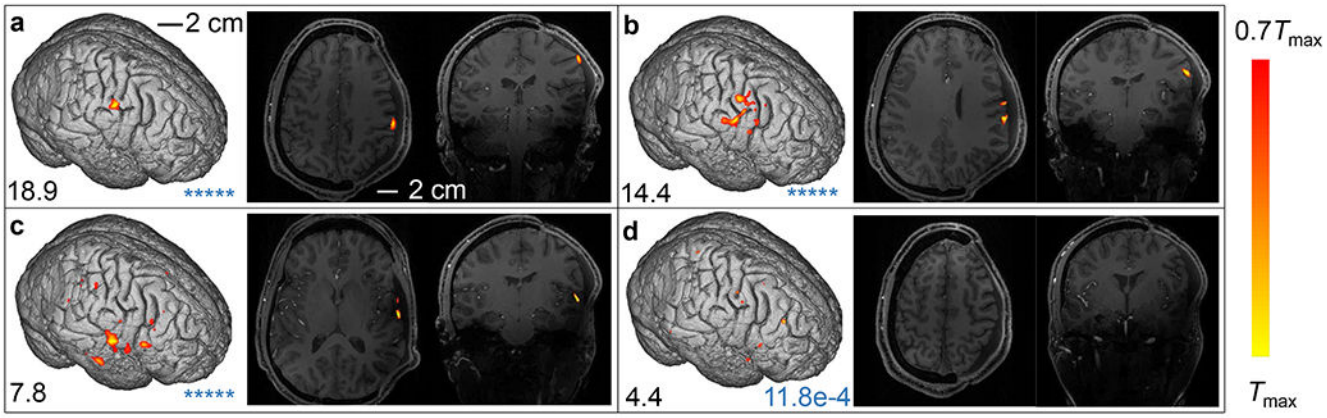

Fig. 5 |. Measuring brain function in a subject who experienced discomfort in MRI due to implants.

a–**d**, Functional responses recorded by the 1K3D-fPACT during LP (**a**), TT (**b**), PL (**c**), and WG (**d**). The maximum *t*-value (in black) is below the cortex. The *p*-value corresponding to 70% maximum *t*-value is displayed (in blue) below the cortex (*****$p < 0.00001$, one-sample one-sided Student's *t*-test, DOF = 222 for fPACT LP and TT, DOF = 207 for fPACT PL and WG, DOF = 142 for fMRI LP and TT, DOF = 132 for fMRI PL and WG, no adjustment; q (FDR) < 0.05 for all maps). LP, TT, PL, and WG were measured twice (see Supplementary Fig. 8).

Table 1

Strengths of the 1K3D-fPACT over BOLD fMRI for cortical neuroimaging.

Mod., modality; cont., contrast; resp., response; BG, Background; sen., sensitivity; line., linearity; port., portability.

Mod.	Cont.	Resp.	BG	Sen.	Line.	Port.	Space	Sound	Costs	Magnet
fMRI	HbR	Early	High	Low	No	No	Closed	Loud	High	Yes
fPACT	HbR, HbO_2, sO_2, CBV	Earlier	Low	High	Yes	Yes	Open	Quiet	Low	No